

Inversion of Love Waves in Earthquake Ground Motion Records for Two-dimensional S-wave Velocity Model of Deep Sedimentary Layers

Kentaro Kasamatsu (✉ kasamake@kajima.com)

Kajima Corporation (Former Tokyo Institute of Technology), 2-19-1 Tobitakyu, Chofu-shi, Tokyo, Japan
<https://orcid.org/0000-0001-9511-5086>

Hiroaki Yamanaka

Tokyo Institute of Technology

Shin'ichi Sakai

The University of Tokyo

Full paper

Keywords: Waveform inversion, Long-period strong motion, Love wave, Two-dimensional assumption, Principal component analysis, S-wave velocity, Deep sedimentary layers, Basin edge, Kanto plain

Posted Date: September 22nd, 2020

DOI: <https://doi.org/10.21203/rs.3.rs-74866/v1>

License:  This work is licensed under a Creative Commons Attribution 4.0 International License.

[Read Full License](#)

Version of Record: A version of this preprint was published on January 12th, 2021. See the published version at <https://doi.org/10.1186/s40623-020-01347-3>.

1 **Title page:**

2 **Title: Inversion of Love Waves in Earthquake Ground Motion Records for Two-**
3 **Dimensional S-wave Velocity Model of Deep Sedimentary Layers**

4

5 Author #1: Kentaro Kasamatsu, Kajima Corporation (Former Tokyo Institute of
6 Technology), 2-19-1 Tobitakyu, Chofu-shi, Tokyo, Japan, kasamake@kajima.com

7 Author #2: Hiroaki Yamanaka, Tokyo Institute of Technology, 4259 Nagatsuta, Midori-
8 ku, Yokohama, Kanagawa, Japan, yamanaka.h.aa@m.titech.ac.jp

9 Author #3: Shin'ichi Sakai, Earthquake Research Institute, The University of Tokyo, 1-
10 1-1 Yayoi, Bunkyo-ku, Tokyo, Japan, coco@eri.u-tokyo.ac.jp

11 **Corresponding author: #1**

12

13

14

15

16

17 **Abstract**

18

19 We have proposed a new waveform inversion method to estimate a 2D S-wave
20 velocity structure of deep sedimentary layers using broadband Love waves. As a
21 preprocessing operation in our inversion scheme, we decompose earthquake observation
22 records into velocity waveforms at periods of 1 s interval. Then, we verify an assumption
23 of 2D propagations of Love waves with polarization features based on a principal
24 component analysis to select the segments applied for the inversion. A linearized iterative
25 inversion analysis for the selected Love wave segments filtered at period of every 1 s
26 allows a detailed estimation of boundary shapes of interfaces over the seismic bedrock
27 with an S-wave velocity of approximately 3 km/s. We demonstrate the technique's
28 effectiveness with applications to observed seismograms in the Kanto plain, Japan.
29 Differences between the estimated and existing structural models are remarkable at basin
30 edges. A regional variation of the near-surface S-wave velocities in our model is similar
31 to a distribution of surface geological classifications. Since a subsurface structure at a
32 basin edge strongly affects earthquake ground motions in a basin with generations of

33 surface waves, our method can provide a detail model of a complex S-wave velocity
34 structure at an edge part for a strong ground motion prediction.

35

36 **Keywords**

37

38 Waveform inversion, Long-period strong motion, Love wave, Two-dimensional
39 assumption, Principal component analysis, S-wave velocity, Deep sedimentary layers,
40 Basin edge, Kanto plain

41

42 **Introduction**

43

44 A prediction of an earthquake ground motion using a theoretical approach such a FD
45 simulation requires an appropriate model of subsurface S-wave and P-wave velocities,
46 density, and attenuation factors. Specially, S-wave velocities of deep sedimentary layers
47 over a seismic bedrock with an S-wave velocity of approximately 3 km/s must be
48 accurately modeled for site-specific long-period ground motion estimations in a large

49 basin. Accordingly, several 3D velocity models have been constructed for large basins in
50 Japan (e.g., Sato et al., 1999; Yamanaka and Yamada, 2006; HERP, 2009; HERP, 2012;
51 Yoshimoto and Takemura, 2014; HERP, 2017). Hereinafter, we refer the models by HERP
52 (2009), HERP (2012), and HERP (2017) as the HERP2009, HERP2012, and HERP2017
53 models, respectively. In particular, the HERP2009 and HERP2012 models cover the
54 whole of Japan. The latter model was constructed from procedures suggested by Koketsu
55 et al. (2012) as an updated version of the HERP2009 model with improvements with
56 additional data such as results of earthquake ground motion simulations and geophysical
57 surveys. The HERP2017 model was constructed only for the Kanto plain based on a
58 model by Senna et al. (2013) who combined a shallow 3D subsurface structural model
59 with deep one which had ever been modeled separately. Senna et al. (2013) established
60 their model with reference to procedures for constructing a 3D structural model indicated
61 by HERP (2017). Digital data of the HERP2009, HERP2012, and HERP2017 models are
62 available for uses in earthquake ground motion evaluations (HERP, 2009; HERP, 2012;
63 HERP, 2017). These velocity models have been validated by comparing simulated
64 earthquake ground motions with observed ones for moderate seismic events. For example,

65 the HERP2017 model was examined for its appropriateness from estimations of
66 goodness-of-fit analyses between synthetic and observed waveforms for several
67 earthquakes.

68 It is well known that details of a velocity structure at a basin edge affect ground
69 motion characteristics in an entire basin due to developments of surface waves. For
70 example, Kawase (1996) showed that a large amplitude area was caused by a constructive
71 interference of direct S-waves and basin-induced Rayleigh waves generated at a basin
72 edge during the 1995 Hyogo-ken Nanbu Earthquake through strong ground motion
73 simulations. The most of the existing 3D models were established by interpolating
74 accumulations of 1D and 2D profiles with several velocity discontinuities from
75 geophysical explorations. These 3D models may lack for detailed features in the edge
76 parts because of difficulties to model their complicated shapes.

77 As one of the alternatives for modeling deep sedimentary layers including a detailed
78 basin-edge structure, inversion analyses using seismograms from moderate events have
79 been performed for 3D basin profiles (e.g., Aoi, 2002; Iwaki and Iwata, 2011). However,
80 such 3D inversions rely on iterative forward calculations for partial derivatives using a

81 3D FD scheme with numerous computational costs. Thus, it takes a long computational
82 time to conduct many inversion analyses using various conditions and initial models.
83 Therefore, a waveform inversion method for retrieving a 2D profile of the deep
84 sedimentary layers from earthquake records can be practically effective because of its
85 low computational costs. As examples of previous studies on the 2D waveform inversions,
86 Aoi et al. (1995) proposed an inversion method with an assumption of a plane incident
87 wave employing a 2D boundary-element method. Ji et al. (2000) set a 1D structural model
88 outside a basin, and performed an inversion analysis to estimate a 2D basin structure by
89 perturbing depths of several control points in numerical experiments. Most of the studies
90 on the 2D waveform inversions examined performances of their methods through the
91 numerical experiments with synthetic ground motions. There are few case studies applied
92 the 2D inversion techniques to observation records (e.g., Zhao et al., 2004; Hikima and
93 Koketsu, 2010). One of the reasons for the difficulty in the application to actual data is
94 approximating the actual 3D wave propagation to the 2D one. For example, Aoi et al.
95 (1997) pointed out that a simple vertically impinged plane-wave might not sufficiently
96 represent the real complex incident wave and causes errors in the 2D inversion results.

97 Hikima and Koketsu (2010) assumed that body and surface wave propagations can be
98 fully reproduced by a 2D modeling. However, they could not adequately verify the
99 assumption of the 2D approximations of the body and surface wave propagations. The
100 violation of the 2D assumption might distort an estimated 2D model from a true velocity
101 structure.

102 In this study, we propose a new waveform inversion method to estimate a 2D S-wave
103 velocity structure of deep sedimentary layers using Love waves from a moderate
104 earthquake. As a preprocessing operation in our method, we first analyze the observation
105 records for the validation of the 2D Love wave propagation assumption to select their
106 segments used in the inversion. We demonstrate our method's applicability to actual data
107 recorded in the Kanto plain, Japan from comparisons of estimated 2D structures with
108 existing models.

109

110 **Earthquake Records**

111

112 Here, we describe characteristics of long-period earthquake ground motion records

113 acquired during a moderate M_J 6.4 (JMA magnitude) earthquake in the Kanto plain, Japan
114 for the use of the later waveform inversion. Figure 1 shows locations of the earthquake
115 epicenter estimated by JMA and seismic observatories whose records are used in this
116 study. The top depths of the seismic bedrock with an S-wave velocity of 3.2 km/s from
117 the HERP2009 model are also illustrated by red contours in the figure. The event is a
118 strike-slip crustal earthquake with a focal depth of 14 km, and has a fault mechanism with
119 a compression axis in the northwest–southeast direction (Fukuyama et al., 1998). Densely
120 distributed strong motion stations have been installed as the parts of strong motion
121 networks such as K-NET, KiK-net (NIED, 2019), and MeSO-net (Hirata et al., 2009) in
122 the study area. The K-NET stations have accelerometers installed on the surface, while
123 there are two accelerometers on the surface and at a depth more than 100 m at the KiK-
124 net stations. Accelerometers at the MeSO-net stations have been installed at a depth of
125 20 m. We used the surface records at the K-NET and KiK-net stations and the borehole
126 records at the MeSO-net stations regarding as the surface motions.

127 The velocity Fourier amplitude spectra at stations of SIT003, TKY007, and E.KNJM
128 are shown in Figure 2 as examples of the observed ground motion records. These stations

129 are located in the areas with the thick sedimentary layers (e.g., Shima, 1977) which can
130 amplify ground motions with a dominant period of approximately 8 s. It is well known
131 that the sediments in the central part of the Kanto plain has a predominant period of 8 s
132 of motions in the previous studies with a focus on long-period surface wave propagations
133 (e.g., Tanaka et al., 1980; Yamanaka et al., 1989; Kinoshita et al., 1992).

134 Figure 3 shows velocity waveforms at eight stations in the northwest–southeast
135 direction, which is almost equal to the transverse direction, along Line-1 from TKY003
136 to E.MZUM. The vertical axis of each panel denotes a distance from TKY003 at the edge
137 of the basin. This distance is hereinafter referred as a basin-edge distance. The velocity
138 waveforms were calculated from the acceleration records by integrating with the fast
139 Fourier transform. A Gaussian band-pass filter represented by Eq. (1) was also applied to
140 the records in the integration at central periods, T^m , of 1, 3, 5, and 9 s for the filtered
141 velocities. This filter shape is expressed as:

$$142 \quad W(T^m) = \exp\left[-\gamma\left\{\frac{(T^m - T^j)}{T^m}\right\}^2\right], \quad (1)$$

143 where T^j represents a discrete period calculated by the Fourier transform. γ is a
144 coefficient for determining the filter width, which is set to 50 with reference to Uetake

145 and Kudo (2001) who investigated characteristics of long-period Love wave propagations
146 at the Kanto area. Figure 3 shows that large amplitude surface waves propagate to the
147 northeast direction, which is almost equal to the radial direction, after arrivals of S-waves.
148 For example, the record at E.IMIM at a period of 3 s has the surface wave arriving
149 approximately at a time of 70 s with much larger amplitude than that of the S-wave. We
150 can also see the surface waves with amplitudes larger than those of the S-waves at the
151 other periods.

152 **Particle motions**

153 Horizontal orbits of the velocity motions at the eight stations along Line-1 are shown
154 in Figure 4a. These orbits are calculated for the segments including the surface waves
155 shown in Figure 3. We use the motions at periods from 1 to 10 s because the surface wave
156 motions are predominant especially in this period range. The particle motions at periods
157 of 1 s interval are arranged from the top to the bottom in Figure 4a. The horizontal axes
158 in the figures denote the basin-edge distances of each station. Principal axis directions
159 evaluated by a principal component analysis (Montalbetti and Kanasewich, 1970) are
160 superimposed with red lines. The motions are polarized in the transverse direction

161 especially at the long-periods such as a period of 10 s. This means that transversely
162 oriented components of the ground motions are mainly Love waves propagating to the
163 radial direction.

164

165 **Methodology for Estimating 2D S-wave Velocity Structure**

166 **Preprocessing**

167 We select the segments used for the waveform inversion by inspecting polarization
168 features of the horizontal particle motions described in the previous section. The
169 amplitudes of the motions in the radial direction become large as the basin-edge distances
170 increase such as in the horizontal motions at SIT003 and E.MZUM at a period of 7 s in
171 Figure 4a. Accordingly, we observe deviations of the principal directions from the
172 transverse direction and increases of the ellipticities of the horizontal particle motions.
173 We also see that the principal axis directions of the particle motions tend to largely differ
174 from the transverse direction at the short-periods. The short-period ground motions may
175 be much influenced by scattering waves due to 3D irregularities. These biases of the
176 principal axis directions of the motions clearly suggest a difficulty in the assumption of

177 the 2D approximation of the Love wave propagations especially at the short-periods. It
 178 is therefore crucial to select band-pass filtered segments of Love wave motions for our
 179 inversion to estimate a 2D S-wave velocity structure. Hereinafter, the assumption of the
 180 2D approximation in the Love wave propagations is referred to two-dimensionality. From
 181 the above analyses of the observed Love waves at each period, we can suppose that the
 182 two-dimensionality is satisfied in the propagation of the long-period Love wave motion
 183 at the stations in the long basin-edge distances.

184 The band-pass filtered segments to be used in the 2D inversion are selected from the
 185 polarization features (e.g., Vidale, 1986). As described above, the propagations of the
 186 short-period Love waves contain non-two-dimensional waves due to the 3D irregularities.
 187 We thus define an E-value to examine the two-dimensionality quantitatively as follows:

$$188 \quad E_i^m = \frac{|\theta_i^m - \theta_i^{ref}|}{90} \cdot |\phi_i^m - \phi_i^{ref}|, (2)$$

189 where θ_i^m and ϕ_i^m represent the principal axis direction and the ellipticity of the
 190 motions calculated by the principal component analyses using the segments in the
 191 transverse and radial directions at the i -th station and the m -th period, respectively. Here,
 192 θ_i^m is measured from -90° to 90° . We suppose that the two-dimensionality of the Love

193 wave propagation is sufficiently satisfied at a period of 10 s because this period is longer
194 than the predominant one of the Love wave amplification expected from the S-wave
195 velocity structure of the deep sedimentary layers as explained earlier. Thus, the principal
196 axis direction θ_i^{ref} and the ellipticity ϕ_i^{ref} of the motions at a period of 10 s are
197 regarded as reference values. The biases of θ_i^m and ϕ_i^m from θ_i^{ref} and ϕ_i^{ref} are used
198 for the E-value E_i^m as their product. The reference period can be set to the longest one
199 considering ratios of the Fourier amplitude spectra between pre-trigger and principal
200 motions of the observation records. We set the reference period to 10 or 9 s in this study.

201 Figure 4b shows the E-values of the Love wave segments at the eight stations along
202 Line-1. The horizontal axes in the figure indicate the basin-edge distances. The E-values
203 at periods from 1 to 9 s are arranged from the top to the bottom. The E-values of the
204 stations at a period of every 1 s are plotted with circles in Figure 4b. The E-values have
205 a clear dependency of the periods. Namely, we see that the long-period segments have
206 the small E-values at the stations far from TKY003. For example, the principal axis
207 direction at a period of 8 s deviates from the transverse direction by approximately 45°
208 at distances more than 50 km (as shown in Figure 4a) with the E-value of approximately

209 0.2. Furthermore, the biases of the principal axis directions of the motions at a period of
210 5 s are also large at distances more than 15 km (as shown in Figure 4a) with E-values of
211 more than 0.2. We therefore considered that the small E-values less than approximately
212 0.2 indicate the satisfaction of the two-dimensionality assumption for the 2D waveform
213 inversion. The maximum basin-edge distances of the stations with E-values less than 0.2
214 at the individual periods are shown by arrows in Figures 4a, 4b, and 4c. In Figure 4c, the
215 horizontal and vertical axes denote the basin-edge distance and the period of the motion,
216 respectively. We also illustrate a range of the basin-edge distances and the periods where
217 the two-dimensionality can be satisfied by a gray-shade area. We use the band-pass
218 filtered segments at periods and distances inside this range for the inversion analysis.

219 The important point of the above preprocessing is that the number of the segments
220 used in the 2D waveform inversion differs depending on the periods of the motions. Table
221 1 shows the numbers of the stations whose E-values are less than 0.2 and the maximum
222 basin-edge distances used in later inversion analyses at each period. The shorter the
223 periods of the Love wave motions are, the smaller the numbers of the segments are used
224 in the inversion. The short-period Love waves at the stations only around the edge part

225 can be used in the 2D inversion, while the long-period Love waves at the stations at
226 distances far from the edge can be used.

227 **Model Parameterization**

228 In the waveform inversion, we assume a homogeneous layered model with irregular
229 interfaces. Boundary shapes of layers in the 2D model are deduced in the inversion of the
230 band-pass filtered segments of the Love wave motions as selected in the preprocessing.
231 Physical parameters such as S-wave and P-wave velocities, density, and attenuation
232 factors are given in advance.

233 We employed a boundary shape parameterization suggested by Aoi et al. (1997). The
234 difference of discretized boundary shapes between present and initial 2D models, $\zeta(x) -$
235 $\zeta_0(x)$, is described by a linear combination of coefficients $p_{n,k}$ and basis functions c_k as in
236 Eq. (3):

$$237 \quad \zeta(x) - \zeta_0(x) = \sum_{k=0}^{K+1} p_{n,k} c_k(x), \quad (3)$$

238 where x denotes a horizontal distance from the left end of the model. Suffixes n and k
239 represent the n -th boundary interface and the k -th basis function, respectively. c_k is
240 common to all the interfaces and represented as follows:

$$\begin{aligned}
241 \quad c_k(x) &= \begin{cases} \frac{1}{2} \left\{ 1 + \cos \frac{\pi}{\Delta} (x - x_k) \right\}, & \text{if } (x_{k-1} \leq x \leq x_{k+1}) \\ 0, & \text{otherwise} \end{cases}, \quad (4) \\
&\quad (k = 1, 2, \dots, K)
\end{aligned}$$

$$\begin{aligned}
242 \quad c_0(x) &= \begin{cases} \sin \frac{\pi}{\Delta} (L + x), & \text{if } (-L \leq x \leq -L + \Delta/2) \\ \frac{1}{2} \left\{ 1 + \cos \frac{\pi}{1 - \Delta/2} (L - \Delta/2 + x) \right\}, & \text{if } (-L + \Delta/2 \leq x \leq -L + \Delta) \\ 0, & \text{otherwise} \end{cases}, \quad (5)
\end{aligned}$$

$$243 \quad c_{K+1}(x) = c_0(-x), \quad (6)$$

244 The model to be estimated has a length of $2L$ in the range of $-L \leq x \leq L$. The model in the
245 horizontal direction is equally divided into $K+1$ pieces with $K+2$ node points that are
246 numbered from 0 to $K+1$. Δ indicates the horizontal interval of the basis functions, which
247 is equal to $2L/K+1$. x_k denotes the horizontal distance of the k -th basis function
248 contributing to the depths at distances from x_{k-1} to x_{k+1} . The $p_{n,k}$ s are unknown parameters
249 in the inversion to minimize residuals between the observed and synthetic Love waves as
250 described in the next subsection.

251 Inversion Method

252 We employed a linearized iterative inversion algorithm using the Gauss-Newton
253 method to obtain an optimized solution. The linearized system to be solved can be

254 expressed as:

$$255 \quad \begin{pmatrix} \mathbf{A} \\ \mathbf{G} \end{pmatrix} \delta \mathbf{p} = \begin{pmatrix} \mathbf{e} \\ \mathbf{0} \end{pmatrix}, (7)$$

256 where $\delta \mathbf{p}$, \mathbf{A} , \mathbf{G} , and \mathbf{e} are the correction matrix, the Jacobian matrix, the smoothing
257 matrix, and the residual matrix, respectively. The partial derivatives of the Jacobian
258 matrix \mathbf{A} can be numerically computed with model perturbations, dp , using the backward
259 FD scheme. dp is set to 2.5 times the vertical FD grid spacing in the 2.5D forward
260 calculation, which is described in the next subsection.

261 The residual matrix \mathbf{e} is defined from the residuals between the observed and synthetic
262 segments. We evaluate the residuals with the L2 norm as follows:

$$263 \quad e = \frac{1}{M} \sum_{m=1}^M \left[\frac{1}{N^m} \sum_{i=1}^{N^m} \left\{ \sum_{j=ts_i^m}^{te_i^m} \left(\frac{o_i^m(t_j) - s_i^m(t_j)}{o_i^m(t_{\max})} \right)^2 \right\} \right], (8)$$

264 where $o_i^m(t_j)$ and $s_i^m(t_j)$ are the observed and synthetic velocities of the Love wave
265 segments selected with the E-values at periods of 1 s interval. Suffixes i , j , and m
266 represent the i -th station, the j -th time interval of the digitized segment, and the m -th
267 period, respectively. The residual between $o_i^m(t_j)$ and $s_i^m(t_j)$ is normalized with the
268 observed maximum amplitude $o_i^m(t_{\max})$ of each band-pass filtered segment. M is the

269 number of the periods. N^m is the number of the stations at the individual periods. ts_i^m
 270 and te_i^m are the start and end times of the segments to be inverted, respectively. The
 271 number of rows of the matrix \mathbf{e} is given by multiplying M with N^m , and the number of
 272 samples of the inverted digitized waveforms.

273 To make the inversion robust, we include the smoothing matrix \mathbf{G} in which
 274 differences between the $p_{n,k}$ and $p_{n,k+1}$ at the n -th boundary interface do not change largely
 275 as follows:

$$276 \quad g = \frac{\beta^2}{L \cdot (K+1)} (p_{n,k} - p_{n,k+1}), \quad (9)$$

277 where L denotes the number of the layer interfaces to be deduced. β is a coefficient for
 278 determining the strength of the smoothing, which is set to 30 in consideration of the
 279 stability of solutions from results of several inversion analyses using different coefficients
 280 in this study. The number of rows of the matrix \mathbf{G} is given by multiplying L with $K+1$.
 281 We solve Eq. (7) using the singular value decomposition method (Lawson and Hanson,
 282 1974) to obtain $\delta\mathbf{p}$ for the optimal $p_{n,ks}$.

283 **Forward FD Modeling**

284 We use a FD staggered-grid formulation of the 2.5D elastic equation of the SH motion

285 (Liner, 1991) with the fourth-order approximation in space and the second-order
286 approximation in time to simulate the Love wave behaviors in the 2D model. Temporal
287 evolutions of a velocity and a stress are solved using the explicit FD scheme. The AI
288 absorbing boundary condition suggested by Clayton and Engquist (1977) and the buffer
289 region (Cerjan et al., 1985) are introduced at the right, left, and bottom edges of our
290 numerical model to reduce non-physical reflections. The top surface is implemented
291 using the improved vacuum formulation suggested by Zeng et al. (2012). An attenuation
292 is introduced by employing the method of Graves (1996) with a reference frequency of
293 0.4 Hz (Kasamatsu and Kato, 2020).

294 A point load is given at horizontal distances more than 20 km from the basin-edge at
295 the top of the bedrock as an external force to generate the Love waves. One of major
296 difficulties in a waveform inversion is a treatment of effects due to a fault rupture process.
297 We therefore not only give the point load far from the basin part but also convolute the
298 observed and synthetic waveforms to solve this problem (e.g., Ji et al., 2000; Amrouche
299 and Yamanaka, 2015). The convoluted waveform $s_i^m(t)$ can be expressed as:

300
$$s_i^m(t) = F^{-1} \left[T_i^m \cdot O_r^m \right], (10)$$

301
$$T_i^m = \frac{|C_i^m|}{|C_r^m|} \frac{C_i^m \cdot C_r^{m*}}{|C_i^m \cdot C_r^{m*}|}, (11)$$

302 where T_i^m is a transfer function at the m -th period defined from the Fourier spectra of
303 the synthetic waveforms at the i -th station, C_i^m , and a reference station, C_r^m , in Eq. (11).
304 An asterisk indicates a complex conjugate of the Fourier spectrum. T_i^m is multiplied to
305 the observed Fourier spectrum of the reference station, O_r^m , to generate the convoluted
306 waveform, $s_i^m(t)$, using the inverse Fourier transform, F^{-1} , as shown in Eq. (10).

307

308 **Result of Line-1**

309 **Inversion Result**

310 We applied our method to the records of the Mt. Fuji region earthquake in 2011
311 ($M_j6.4$) to retrieve 2D S-wave velocity profiles of the deep sedimentary layers for three
312 survey lines shown in Figure 1. Here, we explain the inversion results for Line-1 in detail.

313 We prepared an initial model by HERP (2009) with seven homogenous layers with
314 S-wave velocities of 0.5 to 4.6 km/s. The sediments over the seismic bedrock consist of
315 three layers with S-wave velocities of 0.5, 0.9, and 1.5 km/s. The optimal bottom depth

316 shapes of these three layers were detected from the inversion of the filtered segments of
317 the Love wave motions selected in the previous section (see Figures 4a, 4b, and 4c). Since
318 the HERP2009 model is an old version of the HERP2012 model, we used the HERP2009
319 model as the initial model in the inversion analysis. We then compare our 2D models with
320 the HERP2012 model.

321 We estimated a velocity structure at horizontal distances from 0 to 57 km using the
322 15 basis functions. The horizontal interval of the basis functions, Δ , represented in Eqs.
323 (4) and (5) was approximately 4 km. A total of 45 $p_{n,ks}$ for the three boundaries of the
324 sediments expressed by Eq. (3) were optimized. We used TKY003 as the reference station
325 for the convolution processing. The grid spacings of the 2.5D FD forward modeling were
326 50 m in the horizontal direction and 20 m in the vertical direction. The vertical grid
327 spacing was 50 m at depths more than 5 km to reduce the computational costs.

328 Figure 5 shows the inverted and observed velocity waveforms at periods of 1, 3, 5,
329 and 9 s. The amplitudes of the synthetic motions at a period of 9 s are slightly
330 underestimated at E.MZUM, E.IMIM, and SIT009. However, the overall characteristics
331 at all the periods are well reproduced at every station. Even the observed and inverted

332 motions at relatively short-periods such as 1 and 3 s show high similarities at SIT012,
333 E.KSRM, and E.OKDM. Synthetic waveforms in the initial 2D model (HERP, 2009)
334 were calculated by the forward simulation as shown in Figure 5. These synthetic
335 waveforms at a period of 9 s contain the Love waves with slightly later arrival times than
336 the observed ones at distances more than 47 km. Furthermore, the amplitudes of the
337 synthetic motions at periods of 3 and 5 s in the initial model are overestimated at
338 E.OKDM and E.KSRM.

339 Figure 6 shows the estimated 2D structure along Line-1. Physical parameters of each
340 layer are listed in Table 2. The third layer can be regarded as an outcrop at distances from
341 0 to 5 km. The bottom depth of the first layer becomes deep at distances more than 5 km.
342 Then, it reaches 0.2 km at distances around 10 km. The bottom depth of the first layer
343 becomes shallow at distances from 12 to 25 km, and the second layer exists near the
344 surface at approximately 17 km.

345 The initial model (HERP, 2009) and the HERP2012 model are also shown in Figure
346 6. At distances more than 30 km, all of our estimated boundary depths of the sedimentary
347 layers are shallower than those in the HERP2012 model. The differences between the

348 inverted and HERP2012 models are remarkable in the shallow parts of the basin-edge
349 area. The estimated bottom depth of the second layer becomes shallow at distances less
350 than 10 km and deep at distances more than 10 km. As the results, the estimated bottom
351 interface of the second layer becomes steeper than that in the HERP2012 model at
352 distances from 5 to 15 km. The bottom depth of the first layer becomes shallow slightly
353 around SIT009 in the HERP2012 model, but the top of the second layer does not exist
354 near the surface unlike our results.

355 As above, our obtained 2D profile shows the more irregular structural features around
356 the basin-edge area than the HERP2012 model. This suggests we could model the
357 detailed velocity structure especially in the edge part due to the introduction of the short-
358 period Love waves in the inversion.

359 **Comparison with HERP2017 Model**

360 In the Kanto plain, the HERP2017 model was constructed as a further updated version
361 of the HERP2012 model. The HERP2017 model contains layers with S-wave velocities
362 less than 0.5 km/s, which are not included in the HERP2009 and HERP2012 models. Our
363 inversion results, therefore, cannot be directly compared with the HERP2017 model.

364 However, we can still find a similarity between them around the basin-edge part along
365 Line-1. Figure 7 compares their 2D structural models at distances from 0 to 22 km as the
366 edge part. The top depths of the bedrock in the HERP2017 and our models show a high
367 similarity. On the other hand, our estimated upper depths of the second and third layers
368 with S-wave velocities of 0.9 km/s and 1.5 km/s are different from those of the
369 HERP2017 model.

370 **Comparison with Surface Geological Classifications**

371 The surface geological classifications (Geological Survey of Japan, 2015) around the
372 basin-edge area along Line-1 are indicated in Figure 7. According to the previous study
373 on relations to S-wave velocities with geological ages (Yamamizu et al., 1981), the layers
374 with S-wave velocities of 1.2 to 1.6 km/s and 0.4 to 0.9 km/s belong to Neogene and
375 Quaternary ages, respectively.

376 In the estimated structure, the third layer with an S-wave velocity of 1.5 km/s can be
377 regarded as an outcrop at distances from 0 to 5 km because of the thin thicknesses of the
378 overlying layers. The surface geology in this area mostly belongs to Neogene age. At
379 distances from 5 to 13 km, the estimated bottom depth of the first layer with an S-wave

380 velocity of 0.5 km/s becomes deep gradually away from a station of SIT012. The
381 geological age of the surface formation in this area is categorized as Quaternary with
382 lower terrace sediments. In the estimated structure, the second layer with an S-wave
383 velocity of 0.9 km/s exists near the surface locally at distances around 17 km. Although
384 the surface geology around this part also belongs to Quaternary age, Geological Survey
385 of Japan (2015) reported an existence of middle terrace sediments which are older than
386 the lower terrace ones in this part. Thus, we can confirm qualitatively that the regional
387 variation of the near-surface S-wave velocities in the estimated model is similar to a
388 distribution of the surface geological classifications.

389

390 **Results of Lines-2 and 3**

391 **Line-2**

392 Figure 8a illustrates an inverted 2D velocity structure along Line-2. The horizontal
393 length along Line-2 is approximately 58 km from the basin edge. We used 28 stations
394 along this line in the inversion analysis. Segments of the Love waves used in the inversion
395 were selected at individual periods from 1 to 10 s except for 6 s from the E-values as

396 shown in Table 1. We excluded the segments at a period of 6 s in the inversion because
397 the Fourier amplitude spectrum of the motion at each station has a trough at this period.
398 The horizontal axis in Figure 8a indicates a horizontal distance from the reference station
399 of OK.NKYM, where the seismic bedrock exists near the surface. Each estimated
400 boundary depth is shallower than that in the initial model (HERP, 2009) at almost all the
401 distances. These boundary depths are also shallower than those in the HERP2012 model
402 at distances more than 25 km. We found remarkable differences between the estimated
403 and initial structures in the basin-edge part. The estimated bottom depth of the first layer
404 is shallower than that in the initial model at approximately 10 km, then it gradually
405 deepens away from OK.NKYM. The shape of the bottom interface of the first layer in
406 the edge part is similar to that in the HERP2012 model.

407 **Line-3**

408 Figure 8b shows an inverted 2D velocity structure along Line-3. The horizontal length
409 along Line-3 is approximately 34 km. We used seven records at periods from 1 to 9 s
410 except for 6 s in the inversion analysis as shown in Table 1. The segments at a period of
411 6 s were excluded with the same reason in the Line-2 inversion as explained in the

412 previous subsection. All the boundary depths of the sedimentary layers are significantly
413 shallower than those in the initial model (HERP, 2009) at distances less than 30 km, and
414 they are in good agreement with the HERP2012 model. The second layer with an S-wave
415 velocity of 0.9 km/s exists near the surface at distances from 15 to 20 km. It was reported
416 that the S-wave velocities of the top layers in the deep sediments around this area are 0.7
417 to 0.8 km/s (Yamanaka and Yamada, 2006). Although we do not consider lateral
418 variations of the S-wave velocities, the existence of the second layer with an S-wave
419 velocity of 0.9 km/s near the surface means that our estimated structure has similar
420 features to the surface S-wave variation of the model by Yamanaka and Yamada (2006).
421 The estimated bottom depths of the layers 1 to 3 at distances more than 30 km in our
422 model are almost the same as those of the HERP2009 and HERP2012 models.

423

424 **Effect of Introducing Short-Period Motions**

425

426 We indicated the importance of the preprocessing operation for confirming the two-
427 dimensionality of the Love wave propagations before the 2D waveform inversion with

428 its applications to the earthquake records in the previous sections. As the result of
429 introducing the preprocessing step, we were able to obtain the detailed 2D profiles
430 especially at the edge parts with the introduction of the short-period Love wave motions
431 as well as the long-period ones. In this section, a numerical experiment using synthetic
432 waveforms generated by a 3D computation is performed to examine an effectiveness of
433 the introduction of the short-period motions in the waveform inversion.

434 The synthetic records were generated using the 3D model by HERP (2012) for the
435 numerical test. The ground motions of the Mt. Fuji region earthquake in 2011 ($M_J6.4$)
436 were simulated at the seven stations along Line-3 employing a 3D FD scheme (e.g.,
437 Graves, 1996; Pitarka, 1999). We regard them as the synthetic-earthquake ground motion
438 records. These seven stations are located at the same locations as the actual observatories.
439 A double couple point force with a source mechanism by F-net (Fukuyama et al., 1998)
440 was given as an external force at the hypocenter location. Fault parameters such as a
441 seismic moment are listed in Figure 1. The HERP2012 model used in the 3D calculation
442 was discretized with a horizontal grid spacing of 100 m and a vertical grid spacing of 10
443 m.

444 We performed two inversion analyses to model sedimentary layers from 0 to 34 km
445 along Line-3 using the synthetic records at periods from 1 to 9 s and from 7 to 9 s,
446 respectively. Then, we compare retrieved 2D profiles from the two inversions with the
447 above true one (HERP, 2012). In the former inversion, the segments at periods from 1 to
448 9 s selected from the E-values were inverted as the same as the inversion using actual
449 observation records in the previous section. In the latter inversion, only the segments at
450 periods of 7 to 9 s were used at entire the distances from 0 to 34 km without consideration
451 of E-values. Other conditions in the two inversions were the same as those in the
452 inversion described in the previous section.

453 The 2D profile from the inversion using the segments at periods from 1 to 9 s is
454 illustrated in Figure 9 with the true structure (HERP, 2012). The true model is well
455 reconstructed by the inversion. The 2D velocity structure estimated using the segments
456 at periods from 7 to 9 s is also shown in Figure 9. Obvious differences are observed
457 between the estimated and true structures at the basin-edge part. The bottom depth of the
458 first layer estimated using only the long-period segments is shallower than that of the true
459 structure at distances from 0 to 15 km. Furthermore, the upper depths of the second and

460 third layers in the estimated structure using the segments at periods from 7 to 9 s also
461 become shallow at distances around 5 km. Thus, the inversion using only the long-period
462 Love waves cannot offer the accurate 2D profile at the basin-edge part. The preprocessing
463 operation with the E-values to include the short-period segments in the 2D inversion
464 enhances a reliability of an inverted 2D profile.

465

466 **Discussion and Conclusion**

467

468 We have proposed a waveform inversion method to estimate a 2D S-wave velocity
469 structure of deep sedimentary layers using broadband Love waves. As a preprocessing
470 operation in our inversion scheme, we decompose earthquake observation records into
471 velocity waveforms at periods of 1 s interval for a confirmation of an assumption of 2D
472 propagations of the Love waves with a principal component analysis of horizontal ground
473 motions. Our linearized iterative inversion analysis allows an accurate estimation of
474 boundary shapes from a top depth of a seismic bedrock to a bottom depth of a layer with
475 an S-wave velocity of approximately 0.5 km/s from the segments of the Love wave

476 motions at a period every 1 s which is selected in the preprocessing step.

477 We have demonstrated the effectiveness of our technique with the applications to the
478 observed seismograms in the Kanto plain, Japan. The remarkable differences were
479 observed between our inverted and the existing models (HERP, 2009; HERP, 2012)
480 especially at the basin-edge area. Our method can offer the detailed 2D velocity profiles
481 at the edges due to the introduction of the short-period segments selected from the E-
482 values for the inversions. A velocity structure at a basin edge strongly affects earthquake
483 ground motions in a basin because of generations of surface waves (e.g. Vidale and
484 Helmberger, 1988; Kawase, 1996; Hartzell et al., 2016). 2D profiles including the details
485 of the basin-edge structure along many lines from our proposed inversions can be used
486 to improve the existing 3D models for accurate earthquake ground motion evaluations.

487 In an actual work for a prediction of a strong ground motion from a large earthquake,
488 a lot of the inversion analyses using various conditions are required in estimations of S-
489 wave velocity structures. Since a high-performance computer for the inversions is not
490 always available in the actual work, we have to reduce a calculational cost in a forward
491 calculation as possible. In this study, our 2D inversion employing the 2.5D FD

492 calculations took approximately one day to obtain an optimal solution by performing
493 parallel computing using the open MP algorithm with a conventional PC equipped with
494 four Intel Xeon processors (E7-8891 v4, 2.8GHz). On the other hand, the 3D FD
495 calculation to generate the synthetic records for the numerical test in the previous section
496 took several days with the same conventional PC. This indicates several hundred times
497 differences in the calculation costs between the 2D and 3D inversion analyses. Although
498 the computational costs depend on a PC's performance used in the calculation, it is still
499 difficult to obtain an optimal solution from a 3D waveform inversion in a reasonable
500 computational cost with a conventional PC.

501 The above differences in the computational cost can be very critical to conduct many
502 inversions of records at dense seismic stations in a large basin. Recently, many earthquake
503 observatories have been installed in large basins, especially in seismically active areas.
504 Our 2D inversion technique can be effectively applied to earthquake records along many
505 lines in such the areas with reasonable computational costs.

506

507 **Declarations**

508 **Ethics approval and consent to participate**

509 Not applicable

510 **Consent for publication**

511 Not applicable

512 **List of abbreviations**

513 · HERP: The Headquarters for Earthquake Research Promotion

514 · NIED: National Research Institute for Earth Science and Disaster Resilience

515 · JMA: Japan Meteorological Agency

516 · 3D: Three-dimensional

517 · 2D: Two-dimensional

518 · 2.5D: Two and one-half dimensional

519 · 1D: One-dimensional

520 · FD: finite-difference

521 **Availability of data and materials**

522 The K-NET and KiK-net strong motion data are available at the Web site of strong-

523 motion seismograph networks operated by the NIED (<http://www.kyoshin.bosai.go.jp/>).

524 The MeSO-net strong motion data are available at the Hi-net web site operated by the
525 NIED (<https://hinetwww11.bosai.go.jp/auth/download/cont/?LANG=en>). The JMA
526 catalog data are available at the Hi-net web site operated by the NIED
527 (<http://www.hinet.bosai.go.jp/?LANG=en>).

528 **Competing interests**

529 The authors declare that they have no competing interests.

530 **Funding**

531 This work was supported by JSPS KAKENHI Grant Number JP17K01324

532 **Authors' contributions**

533 KK conducted the analysis. KK and HY drafted the manuscript. All authors read and
534 approved the final manuscript.

535 **Acknowledgements**

536 We would like to thank the NIED for providing earthquake observation record data
537 and the JMA for their catalog data. We used the Generic Mapping Tools (Wessel et al.,
538 2013) for drawing the figures.

539 **Authors' information**

540 Not applicable

541 **Endnotes**

542 Not applicable

543

544 **References**

545

546 · Amrouche, M. and Yamanaka, H. (2015) Two-dimensional shallow soil profiling

547 using time-domain waveform inversion. *Geophysics* 80(1):EN27-EN41,

548 doi:10.1190/geo2014-0027.1

549 · Aoi, S., Iwata, T., Irikura, K., and Sanchez-Sesma, J. (1995) Waveform inversion for

550 determining the boundary shape of a basin structure. *Bull. Seism. Soc. Am.*

551 85(5):1445-1455

552 · Aoi, S., Iwata, T., Fujiwara, H., and Irikura, K. (1997) Boundary shape waveform

553 inversion for two-dimensional basin structure using three-component array data of

554 plane incident wave with an arbitrary azimuth. *Bull. Seism. Soc. Am.* 87(1):222-233

555 · Aoi, S. (2002) Boundary shape waveform inversion for estimating the depth of three-

556 dimensional basin structures. Bull. Seism. Soc. Am. 92(6):2410-2418,
557 doi:10.1785/0120010245

558 · Cerjan, C., Kosloff, D., Kosloff, R., and Reshef, M. (1985) A nonreflecting boundary
559 condition for discrete acoustic and elastic wave equations. Geophysics 50(4):705-
560 708, doi:10.1190/1.1441945

561 · Clayton, R. and Engquist, B. (1977) Absorbing boundary conditions for acoustic and
562 elastic wave equations, Bull. Seism. Soc. Am. 67(6):1529-1540

563 · Fukuyama, E., Ishida, M., Douglas, S., and Kawai, H. (1998) Automated seismic
564 moment tensor determination by using on-line broadband seismic waveforms. Zisin
565 (Journal of the Seismological Society of Japan. 2nd ser.) 51(1):149-156, doi:
566 10.4294/zisin1948.51.1_149 (in Japanese with English abstract)

567 · Geological Survey of Japan, AIST (ed.) (2015) Seamless digital geological map of
568 Japan 1: 200,000. May 29, 2015 version. Geological Survey of Japan, National
569 Institute of Advanced Industrial Science and Technology.

570 · Graves, R. (1996) Simulating seismic wave propagation in 3D elastic media using
571 staggered-grid finite differences. Bull. Seism. Soc. Am. 86(4):1091-1106

- 572 · Hartzell, S., Leeds, L., Ramirez-Guzman, L., Allen, and P., Schmitt, G. (2016)
573 Seismic site characterization of an urban sedimentary basin, Livermore Valley,
574 California: Site response, basin-edge-induced surface waves, and 3D simulations.
575 Bull. Seism. Soc. Am. 106(2):609-631, doi:10.1785/0120150289
- 576 · Hikima, K. and Koketsu., K (2010) Waveform inversion for 2-D velocity structures
577 and construction of 3-D velocity structure using its results. Abstracts of the 13th Japan
578 Earthquake Engineering Symposium, International Congress Center Epochal
579 Tsukuba, Ibaraki, 17-20 November 2010 (in Japanese with English abstract)
- 580 · Hirata, N., Sakai, S., Sato, H., Satake, K., and Koketsu, K. (2009) An outline of the
581 special project for earthquake disaster mitigation in the Tokyo Metropolitan Area -
582 subproject 1: Characterization of the plate structure and source faults in and around
583 the Tokyo Metropolitan area. Bulletin of the Earthquake Research Institute,
584 University of Tokyo 84(2):41-56 (in Japanese with English abstract)
- 585 · Iwaki, A. and Iwata, T. (2011) Estimation of three-dimensional boundary shape of
586 the Osaka sedimentary basin by waveform inversion. Geophys J Int 186(3):1255-
587 1278, doi:10.1111/j.1365-246X.2011.05102.x

- 588 · Ji, C., Helmberger, D., and Wald, D. (2000) Basin structure estimation by waveform
589 modeling: Forward and inverse methods. *Bull. Seism. Soc. Am.* 90(4):964-976,
590 doi:10.1785/0119990080
- 591 · Kasamatsu, K. and Kato, K. (2020) Long period ground motion simulation of the
592 2011 off the Pacific coast of Tohoku Earthquake using theoretical Green's function:
593 Examination based on inverted pseudo point source model. *Journal of Structural and*
594 *Construction Engineering* 85(769):427-437, doi:10.3130/aijs.85.427 (in Japanese)
- 595 · Kawase, H. (1996) The cause of the damage belt in Kobe: “The Basin-Edge Effect,”
596 constructive interference of the direct s-wave with the basin-induced diffracted/
597 Rayleigh waves. *Seis. Res. Lett.* 67(5):25-34, doi:10.1785/gssrl.67.5.25
- 598 · Kinoshita, S., Fujiwara, H., Mikoshiba, T., and Hoshino, T. (1992) Secondary love
599 waves observed by a strong- motion array in the Tokyo Lowlands, Japan. *Journal*
600 *Physics Earth* 40(1):99-116, doi:10.4294/jpe1952.40.99
- 601 · Koketsu., K., Miyake, H., and Suzuki, H. (2012) Japan integrated velocity structure
602 model version 1. Abstracts of Proceedings of the fifteenth World Conference on
603 Earthquake Engineering, Lisbon, Portugal, 24-28 September 2012

- 604 · Lawson, C. and Hanson, R. (1974) Solving least squares problems. Society for
605 Industrial and Applied Mathematics Classics in Applied Mathematics 15, doi:
606 10.1137/1.9781611971217
- 607 · Liner, L. (1991) Theory of a 2.5-D acoustic wave equation for constant density media.
608 Geophysics 56(12):2114-2117, doi:10.1190/1.1888858
- 609 · Montalbetti, F. and Kanasevich, R. (1970) Enhancement of teleseismic body phases
610 with a polarization filter. Geophysical Journal International 21(2):119-129,
611 doi:10.1111/j.1365-246X.1970.tb01771.x
- 612 · National Research Institute for Earth Science and Disaster Resilience (2019) NIED
613 K-NET, KiK-net. National Research Institute for Earth Science and Disaster
614 Resilience, doi:10.17598/NIED.0004
- 615 · Pitarka, A. (1999) 3D Elastic finite-difference modeling of seismic motion using
616 staggered grids with nonuniform spacing. Bull. Seism. Soc. Am. 89(1):54-68
- 617 · Sato, T., Graves, R., and Somerville, G. (1999) Three-dimensional finite-difference
618 simulations of long-period strong motions in the Tokyo metropolitan area during the
619 1990 Odawara earthquake (M_J 5.1) and the great 1923 Kanto earthquake (M_S 8.2) in

620 Japan. Bull. Seism. Soc. Am. 89(3):579-607

621 · Senna, S., Maeda, T., Inagaki, Y., Suzuki, H., Matsuyama, H., and Fujiwara, H.

622 (2013) Modeling of the subsurface structure from the seismic bedrock to the ground

623 surface for a broadband strong motion evaluation. Journal of Disaster Research

624 8(5):889-903, doi:10.20965/jdr.2013.p0889

625 · Shima, E. (1977) On the deep underground structure of Tokyo Metropolitan Area.

626 Abstracts of Proceedings of the sixth World Conference on Earthquake Engineering,

627 New Delhi, India, 10-14 January 1977

628 · Tanaka, T., Yoshizawa, S., and Osawa, Y. (1980) Characteristics of strong earthquake

629 ground motion in the period range from 1 to 15 seconds, Abstract of Proceedings of

630 the seventh World Conference on Earthquake Engineering, Istanbul, Turkey, 8-13

631 September 1980

632 · The Headquarters for Earthquake Research Promotion (2009) Seismic Hazard Map

633 for the Long-period Ground Motion, the Trial Version in 2009 (Choshuki Jishindo

634 Yosoku Chizu 2009 Shisakuban) (in Japanese).

635 https://www.jishin.go.jp/evaluation/seismic_hazard_map/lpshm/09_choshuki/.

- 636 Accessed 11 Apr 2016
- 637 · The Headquarters for Earthquake Research Promotion (2012) Seismic Hazard Map
638 for the Long-period Ground Motion, the Trial Version in 2012 (Choshuki Jishindo
639 Yosoku Chizu 2012 Shisakuban) (in Japanese).
640 https://www.jishin.go.jp/evaluation/seismic_hazard_map/lpshm/12_choshuki/.
- 641 Accessed 2 May 2016
- 642 · The Headquarters for Earthquake Research Promotion (2017) Kantou Chihouno
643 Senbu Sinbu Tougou Jibankouzou Moderu (in Japanese).
644 [https://www.jishin.go.jp/evaluation/strong_motion/underground_model/integration
645 _model_kanto/](https://www.jishin.go.jp/evaluation/strong_motion/underground_model/integration_model_kanto/).
- 646 Accessed 6 Apr 2020
- 647 · Uetake, T. and Kudo, K. (2001) Three dimensional S-wave velocity structure in and
648 around Ashigara valley, west of Kanagawa prefecture, Japan, evaluated from love
649 wave dispersion data. Zisin (Journal of the Seismological Society of Japan. 2nd ser.)
650 54(2):281-297, doi:10.4294/zisin1948.54.2_281 (in Japanese with English abstract)
- 651 · Vidale, E. (1986) Complex polarization analysis of particle motion. Bull. Seism. Soc.

652 Am. 76(5):1393-1405

653 · Vidale, E. and Helmberger, V. (1988) Elastic finite-difference modeling of the 1971

654 San Fernando, California earthquake. Bull. Seism. Soc. Am. 78(1):122-141

655 · Wessel P, Smith WHF, Scharroo R, Luis J, and Wobbe F (2013) Generic mapping

656 tools: improved version released. EOS Trans AGU 94:409,

657 doi:10.1002/2013EO450001

658 · Yamamizu, F., Takahashi, H., Goto, N., and Ohta, Y. (1977) Shear wave velocities in

659 deep soil deposits Part III: Measurements in the borehole of the Fuchu observatory

660 to the depth of 2,750 m and a summary of the results. Zisin (Journal of the

661 Seismological Society of Japan. 2nd ser.) 34(4):465-479, doi:

662 10.4294/zisin1948.30.4_415 (in Japanese with English abstract)

663 · Yamanaka, H., Seo, K., and Samano, T. (1989) Effects of sedimentary layers on

664 surface-wave propagation. Bull. Seism. Soc. Am. 79(3):631-644

665 · Yamanaka, H. and Yamada, N. (2006) Modeling 3D S-wave velocity structure of

666 Kanto basin for estimation of earthquake ground motion. Butsuri-Tansa 59(6):549-

667 560, doi:10.3124/segj.59.549 (in Japanese with English abstract)

- 668 · Yoshimoto, K. and Takemura, S. (2014) Surface wave excitation at the northern edge
669 of the Kanto Basin, Japan. *Earth, Planets and Space* 66(16), doi:10.1186/1880-5981-
670 66-16
- 671 · Zeng, C., Xia, J., Miller, R., and Tsoflias, G. (2012) An improved vacuum
672 formulation for 2D finite-difference modeling of Rayleigh waves including surface
673 topography and internal discontinuities. *GEOPHYSICS* 77(1):T1-T9,
674 doi:10.1190/geo2011-0067.1
- 675 · Zhao, L., Zheng, T., and Xu, W. (2004) Modeling the Jiyang depression, northern
676 China, using a wave-field extrapolation finite-difference method and waveform
677 inversion. *Bull. Seism. Soc. Am.* 94(3):988-1001, doi:10.1785/0120030167

678

679 **Figure Legends**

680

- 681 · **Fig. 1.** Locations of epicenter and strong ground motion observatories used in this
682 study indicated by focal sphere and squares, respectively. Red contours denote top
683 depths of seismic bedrock modeled by HERP (2009). 2D S-wave velocity structures

684 of deep sedimentary layers were estimated along Line-1 to Line-3 as represented
685 with black thick lines.

686 · **Fig. 2.** Fourier amplitude spectra observed at three stations. Each line shows a
687 spectrum in the normal direction along Line-1 to Line-3 in Figure 1. These spectra
688 are smoothed using the Parzen window with a bandwidth of 0.02 Hz.

689 · **Fig. 3.** Observed velocity waveforms in transverse direction. These waveforms are
690 band-pass filtered at periods of 1, 3, 5, and 9 s. Solid triangles and circles indicate
691 arrival times of P-waves and S-waves, respectively. Vertical axes denote basin-edge
692 distances.

693 · **Fig. 4.** Results of principal component analyses for records along Line-1. (a)
694 Horizontal particle motions and principal axis directions indicated with black and
695 red lines, respectively. The horizontal axis indicates a basin-edge distance. (b) E-
696 values for observatories at individual periods. Waveforms at stations located within
697 distances indicated by arrows are used in 2D inversion analysis. (c) Relationship
698 between periods of ground motions and basin-edge distances for a confirmation of a
699 two-dimensionality in 2D inversion.

700 · **Fig. 5.** Comparison between observed and calculated velocity waveforms at periods
701 of 1, 3, 5, and 9 s along Line-1. Black, red, and blue dotted lines represent observed,
702 inverted, and synthetic waveforms, respectively. The synthetic waveforms were
703 generated from initial model by HERP (2009).

704 · **Fig. 6.** Comparison of inverted 2D velocity structure with previous models. Red,
705 gray dotted, and black lines represent the estimated structure and structural models
706 by HERP (2009, 2012) along Line-1, respectively. The horizontal axis indicates a
707 basin-edge distance. Triangles denote observatory locations.

708 · **Fig. 7** Comparison of 2D velocity structural models around a basin-edge area along
709 Line-1. Red and black lines denote the inverted model and the model by HERP
710 (2017), respectively. S-wave velocities (V_s) denoted by black lines represent those
711 of the model by HERP (2017). Surface geological classifications (Geological Survey
712 of Japan, 2015) are also indicated with gray, black broken, and black solid lines on
713 the top of the models.

714 · **Fig. 8.** Inverted 2D velocity structures along (a) Line-2 and (b) Line-3. Legends of
715 the figures are the same as Figure 6.

716 · **Fig. 9.** Comparison of 2D velocity structures in a numerical test. Gray line represents
717 true structure (HERP, 2012). Black solid and dotted lines indicate inverted structures
718 from band-pass filtered segments at periods from 1 to 9 s and from 7 to 9 s,
719 respectively.

720

721 **Table Legends**

722

723 · **Table 1.** Number of stations and maximum basin-edge distances used in inversion
724 analyses along Lines-1 to 3 at each period.

725 · **Table 2.** Physical parameters of layers 1–4 in Figures 6, 7, 8a, 8b, and 9.

726

Figures

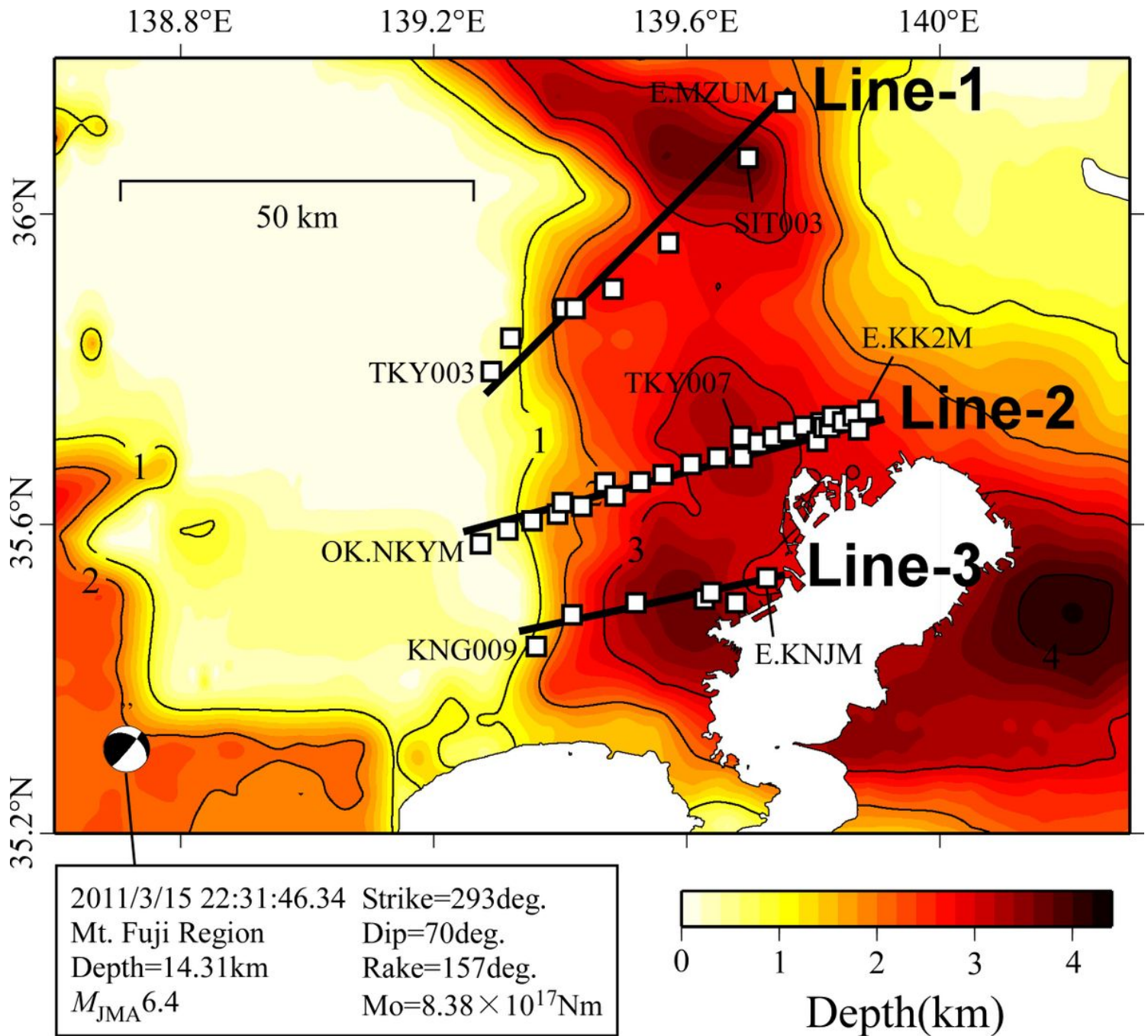


Figure 1

Locations of epicenter and strong ground motion observatories used in this study indicated by focal sphere and squares, respectively. Red contours denote top depths of seismic bedrock modeled by HERP (2009). 2D S-wave velocity structures of deep sedimentary layers were estimated along Line-1 to Line-3 as represented with black thick lines.

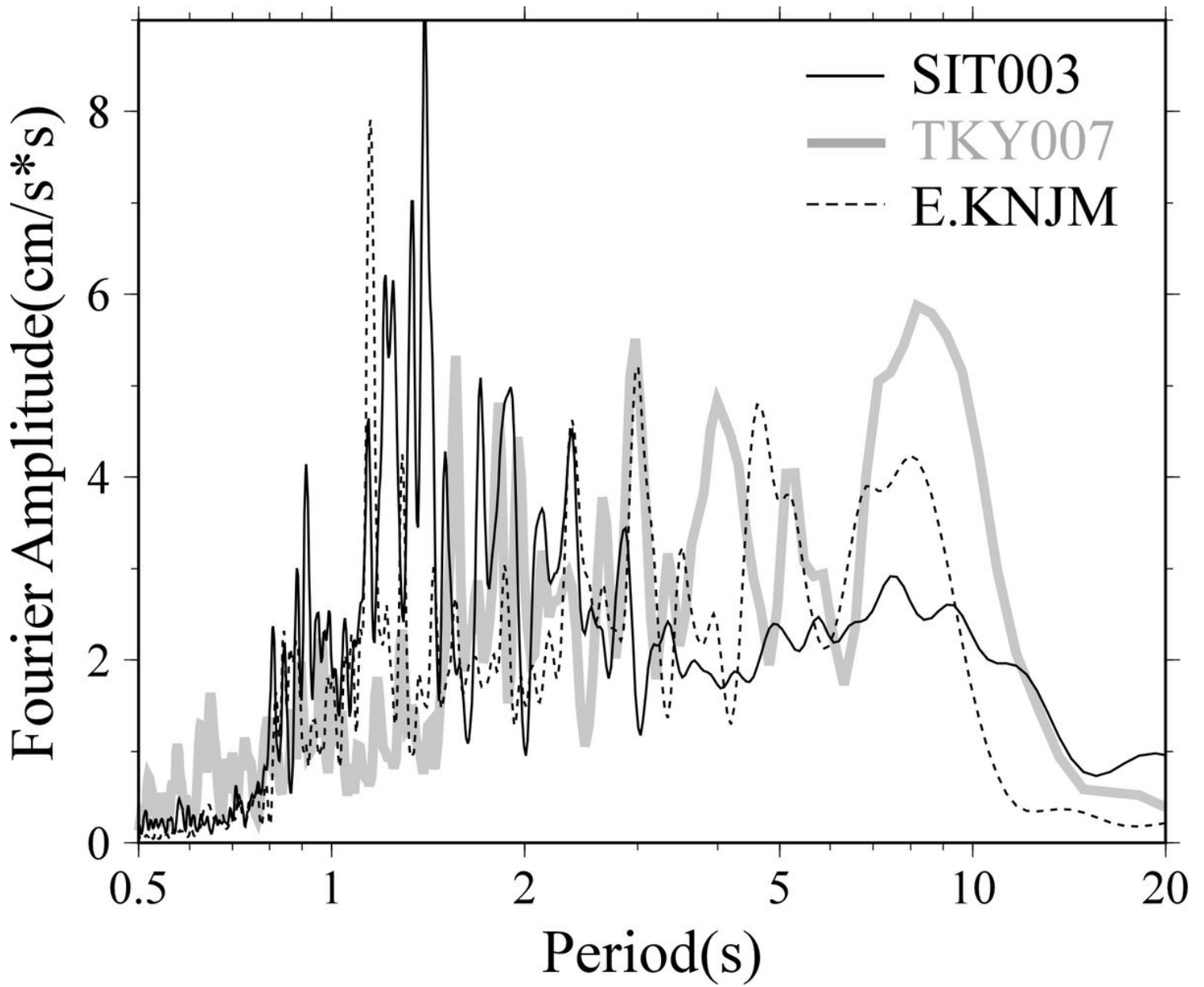


Figure 2

Fourier amplitude spectra observed at three stations. Each line shows a spectrum in the normal direction along Line-1 to Line-3 in Figure 1. These spectra are smoothed using the Parzen window with a bandwidth of 0.02 Hz.

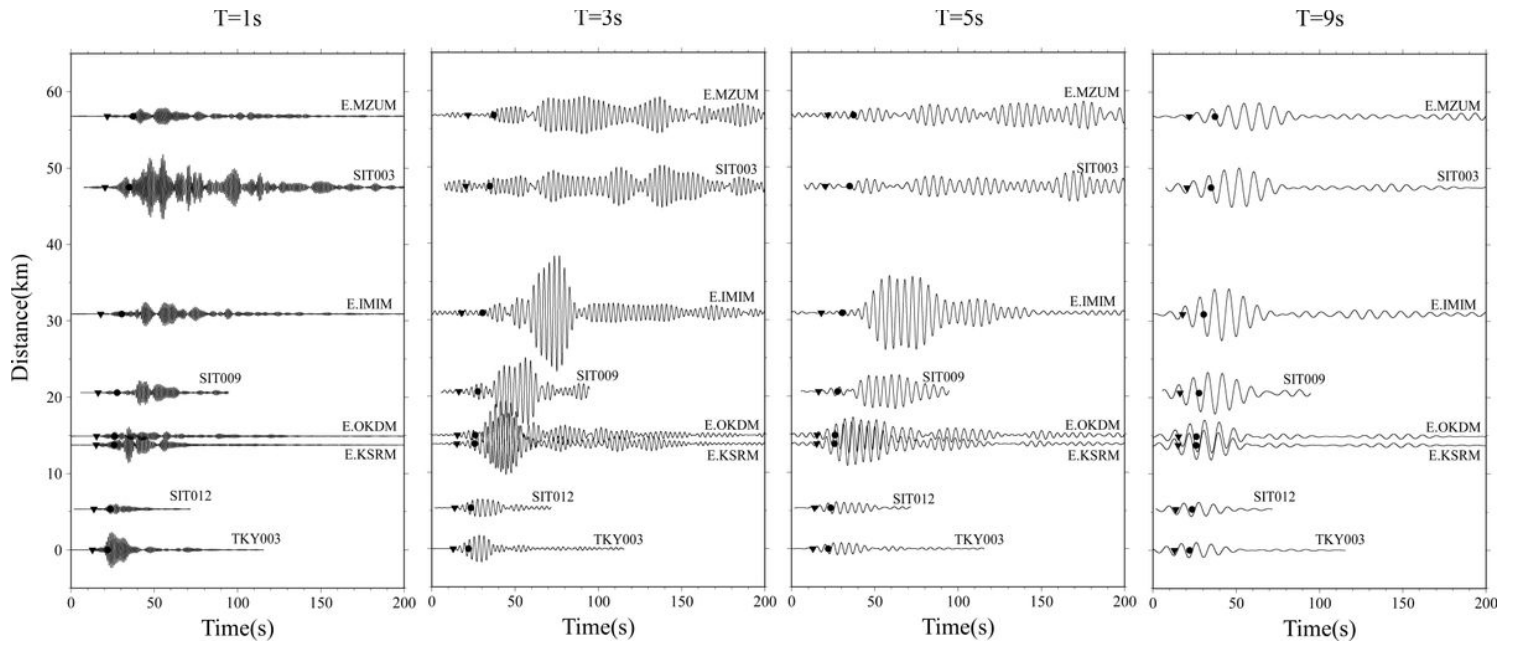


Figure 3

Observed velocity waveforms in transverse direction. These waveforms are band-pass filtered at periods of 1, 3, 5, and 9 s. Solid triangles and circles indicate arrival times of P-waves and S-waves, respectively. Vertical axes denote basin-edge distances.

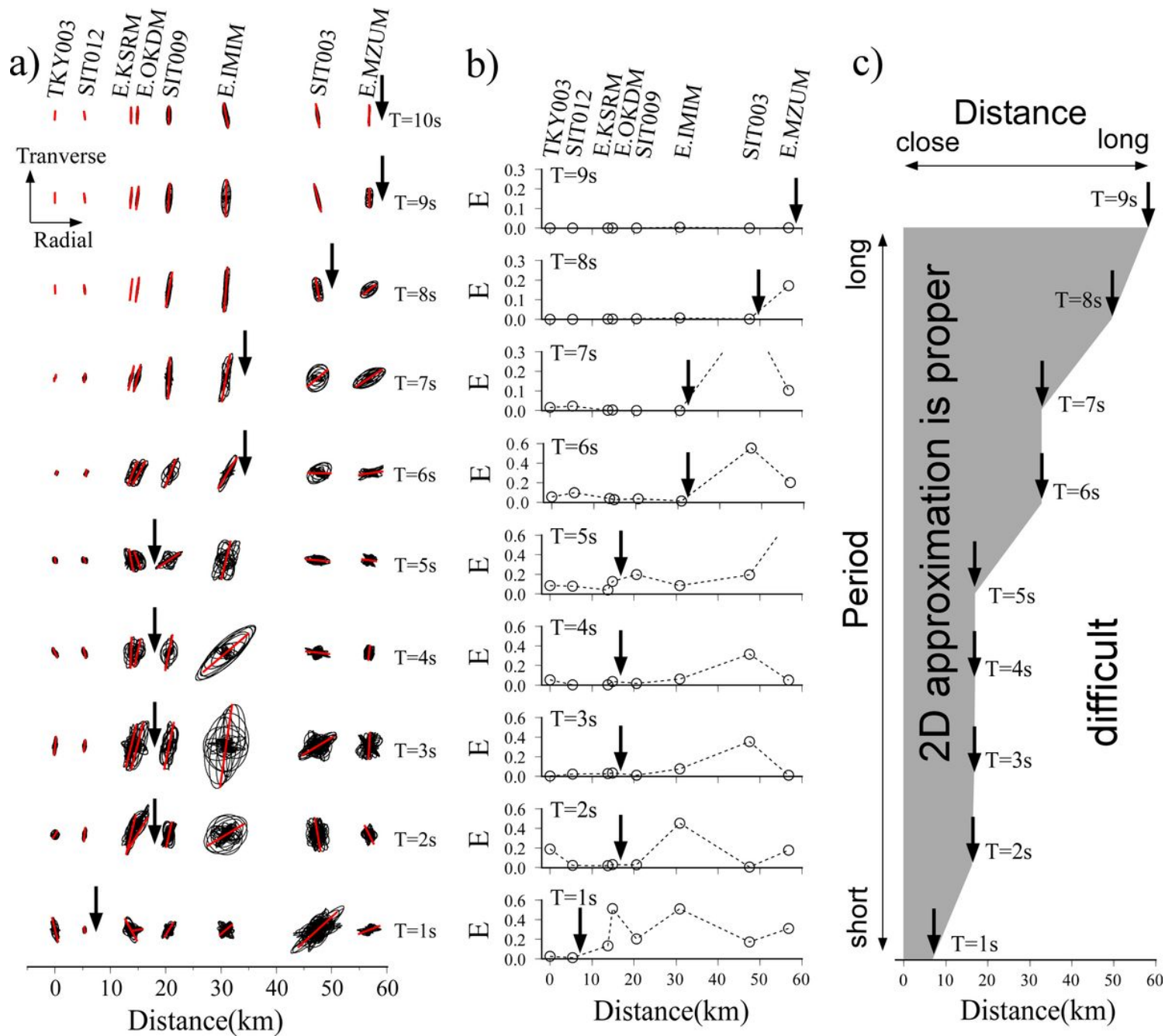


Figure 4

Results of principal component analyses for records along Line-1. (a) Horizontal particle motions and principal axis directions indicated with black and red lines, respectively. The horizontal axis indicates a basin-edge distance. (b) E-values for observatories at individual periods. Waveforms at stations located within distances indicated by arrows are used in 2D inversion analysis. (c) Relationship between periods of ground motions and basin-edge distances for a confirmation of a two-dimensionality in 2D inversion.

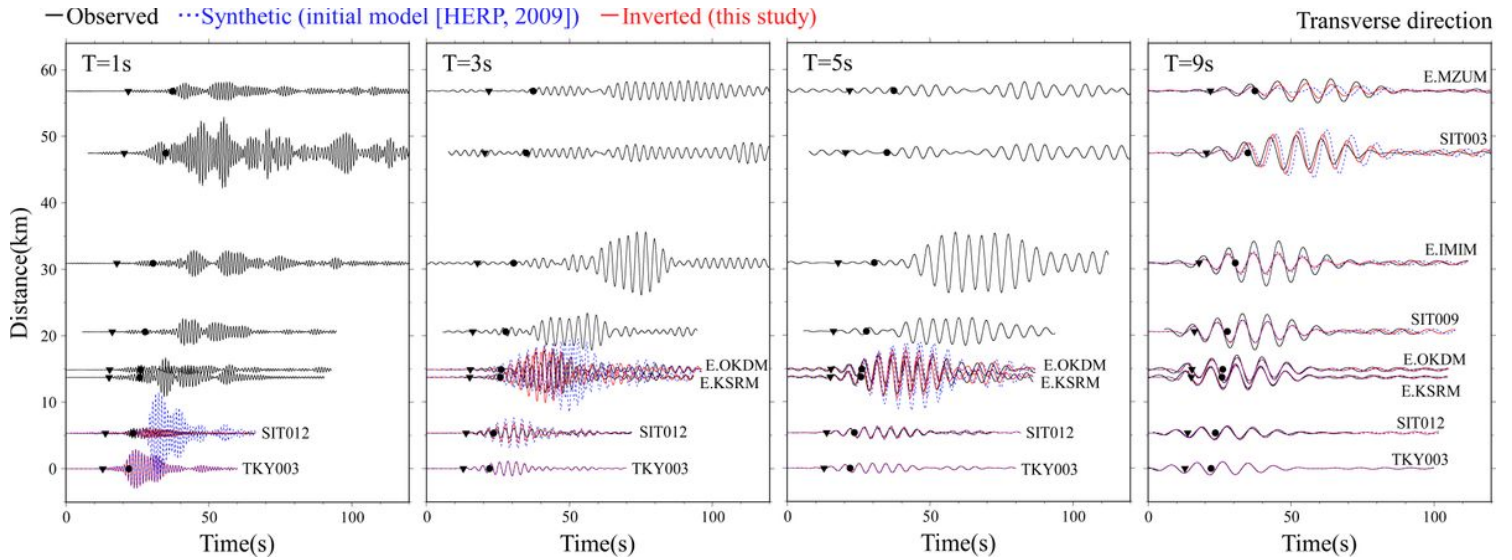


Figure 5

Comparison between observed and calculated velocity waveforms at periods of 1, 3, 5, and 9 s along Line-1. Black, red, and blue dotted lines represent observed, inverted, and synthetic waveforms, respectively. The synthetic waveforms were generated from initial model by HERP (2009).

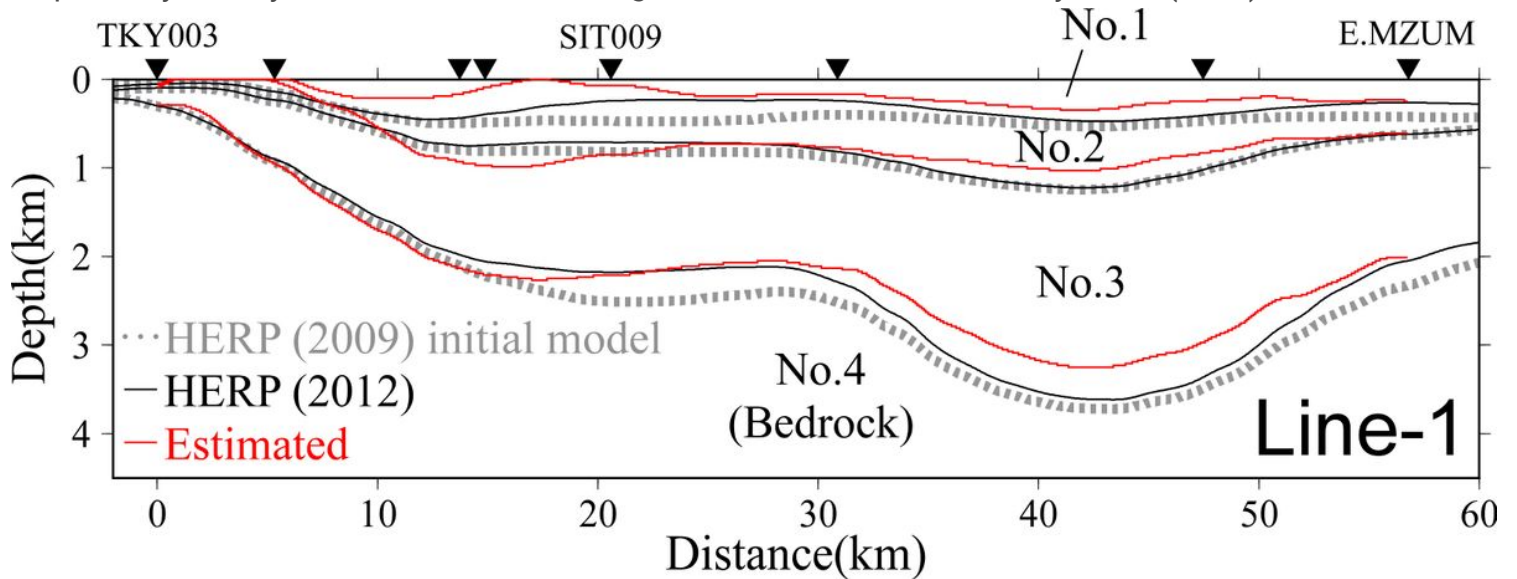


Figure 6

Comparison of inverted 2D velocity structure with previous models. Red, gray dotted, and black lines represent the estimated structure and structural models by HERP (2009, 2012) along Line-1, respectively. The horizontal axis indicates a basin-edge distance. Triangles denote observatory locations.

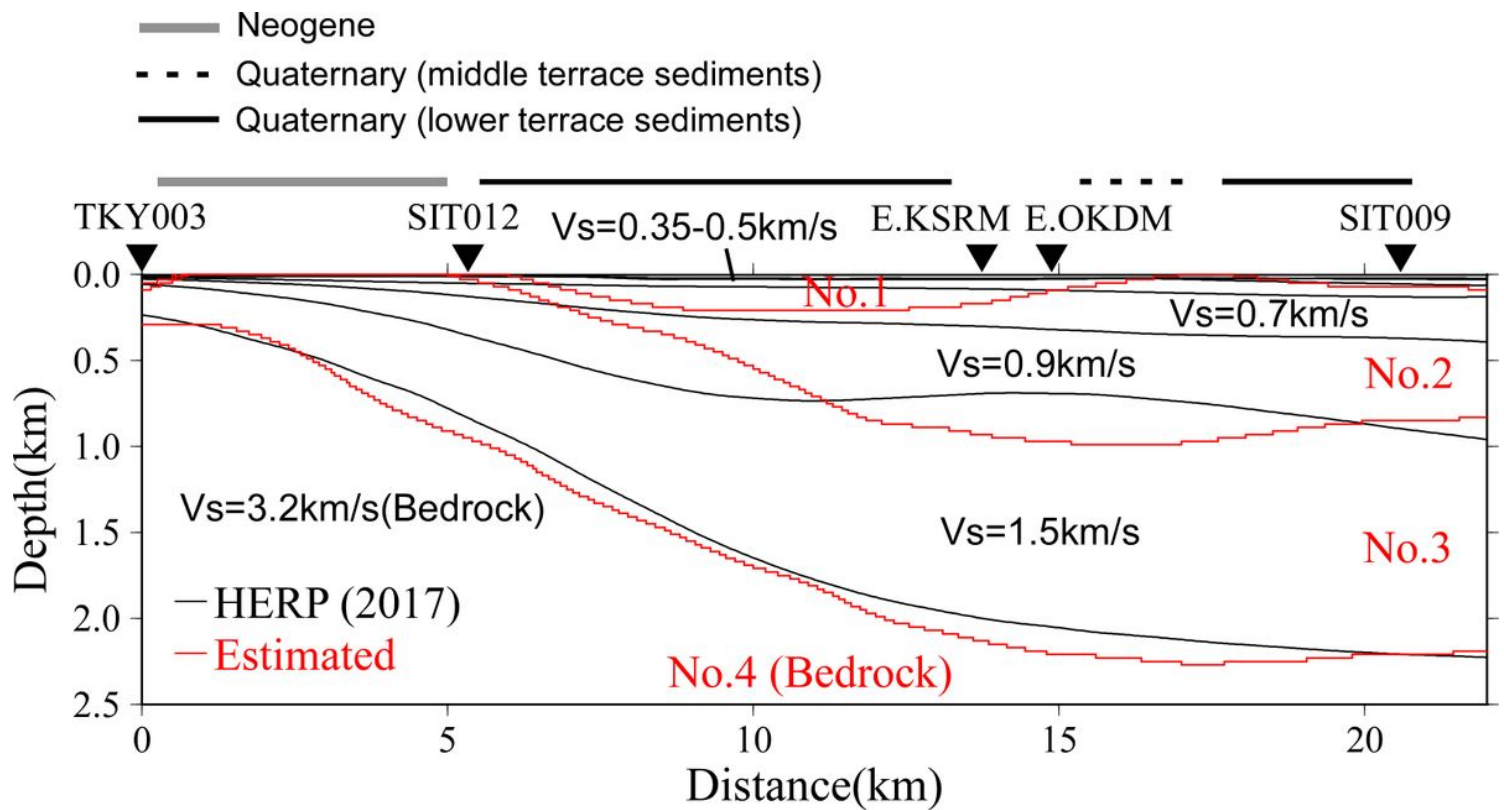


Figure 7

Comparison of 2D velocity structural models around a basin-edge area along Line-1. Red and black lines denote the inverted model and the model by HERP (2017), respectively. S-wave velocities (V_s) denoted by black lines represent those of the model by HERP (2017). Surface geological classifications (Geological Survey of Japan, 2015) are also indicated with gray, black broken, and black solid lines on the top of the models.

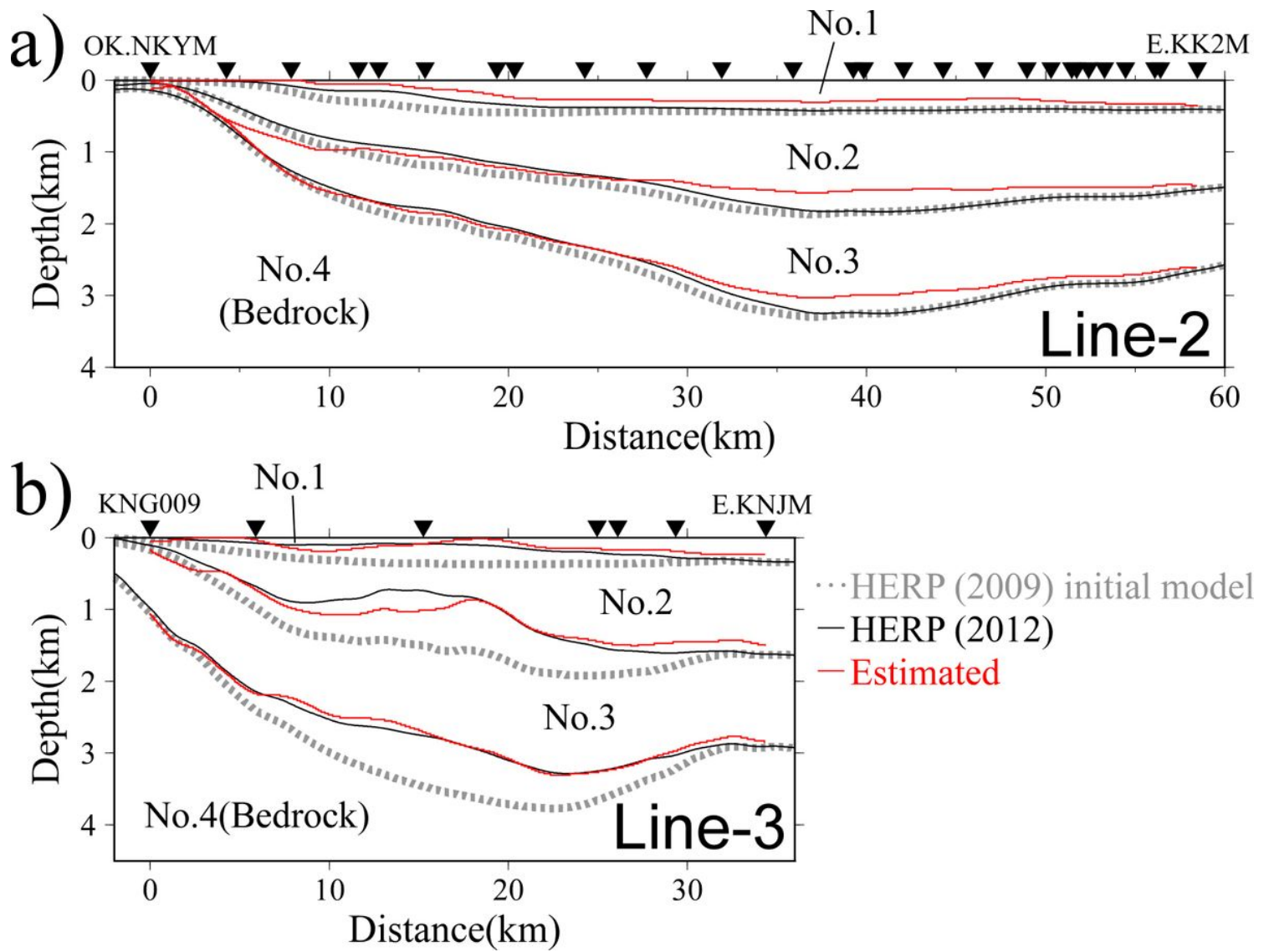


Figure 8

Inverted 2D velocity structures along (a) Line-2 and (b) Line-3. Legends of the figures are the same as Figure 6.

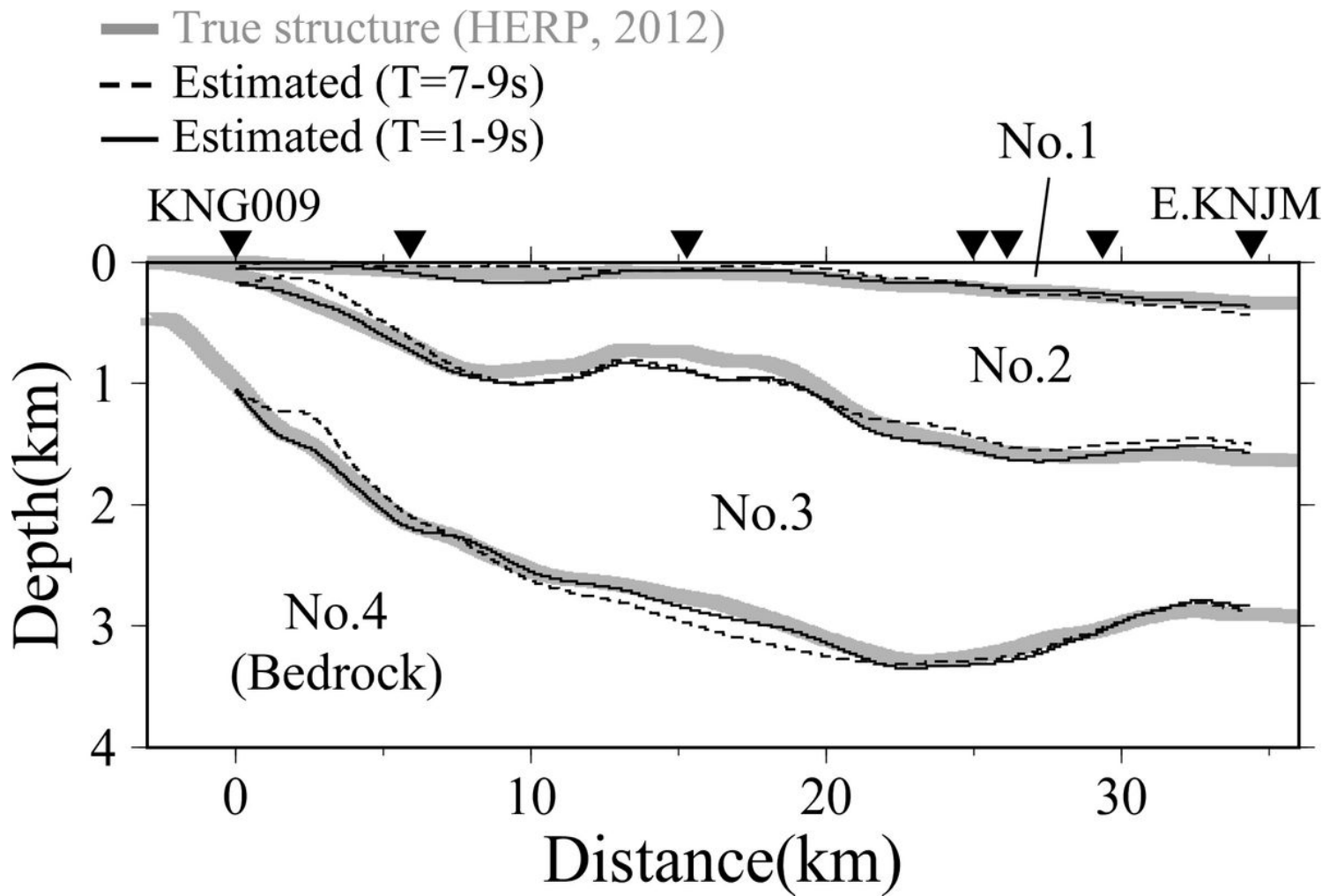


Figure 9

Comparison of 2D velocity structures in a numerical test. Gray line represents true structure (HERP, 2012). Black solid and dotted lines indicate inverted structures from band-pass filtered segments at periods from 1 to 9 s and from 7 to 9 s, respectively.

Supplementary Files

This is a list of supplementary files associated with this preprint. Click to download.

- [GraphicalAbstract.png](#)